Journal of the Physical Society of Japan **83**, 064711 (2014)
http://dx.doi.org/10.7566/JPSJ.83.064711

Andreev Reflection in Weyl Semimetals

Shuhei Uchida[1], Tetsuro Habe[1], and Yasuhiro Asano[1,2]

[1]*Department of Applied Physics, Hokkaido University, Sapporo 060-8628, Japan*
[2]*Center for Topological Science and Technology, Hokkaido University, Sapporo 060-8628, Japan*

(Received March 5, 2014; accepted April 24, 2014; published online May 27, 2014)

We theoretically study low energy electric transport in a junction consisting of a Weyl semimetal and a metallic superconductor. The characteristic features of the differential conductance depend on the relative directions between the current and the vector connecting the two Weyl points. When the electric current is perpendicular to the vector, the conductance spectra are sensitive to the direction and the amplitude of magnetic moment at the junction interface. This is a direct consequence of the chiral spin configuration on the fermi surface near the Weyl points.

1. Introduction

Weyl semimetals are a novel topological material in three-dimension.[1–7)] In the bulk, Weyl semimetal has the gapless spectra characterized by even number of Weyl points with opposite topological charges in Brillouin zone, which leads to unusual transport properties.[8–15)] Topological properties in these cases result from the separation of the individual Weyl points in the absence of of either time-reversal or inversion symmetry. Various theoretical model has been discussed to realize the semimetal phase.[16–18)] In experiments, the semimetal is realized in multilayers of $GeTe/Sb_2Te_3$[19,20)] and Cd_3As_2.[21–23)] Recently a possibility of superconductivity has been discussed in several theoretical studies.[24–26)] Unconventional Cooper pairing symmetry would be expected because of the chiral spin structure on the fermi surface. Although finding the superconductivity within existing semimetals might be difficult, realizing the superconducting correlation there is basically possible by injecting Cooper pairs due to the proximity effect.[27)] As the first step in this research direction, we address the Andreev reflection in Weyl semimetal in the present paper.

In this paper, we theoretically study the low energy transport through a junction consisting a Weyl semimetal and a metallic superconductor. The differential conductance of the Wely-semimetal/superconductor junction is calculated from the normal and the Andreev reflection coefficients of the junction. We consider a 2×2 simple Hamiltonian which describes the electronic structure of a Weyl semimetal breaking the time-reversal symmetry. Within this model, the semimetallic excitation is characterized by the linear energy-momentum dispersion relations near the two separated Weyl points. The spin structures at the two fermi surfaces are characterized by the opposite spin chiral texture to each other. When the two Weyl points stay at $\pm\boldsymbol{K}_0$ with $\boldsymbol{K}_0 = (0, 0, k_0)$, the topological surface states appears on the four surfaces parallel to $\boldsymbol{K}_0$ direction. We consider two types of junction: the current parallel to $\boldsymbol{K}_0$ and the current perpendicular to $\boldsymbol{K}_0$. When the potential barrier at the interface is spin-independent, the conductance spectra in the junctions are similar to those in the usual normal-metal/superconductor junctions. When the potential at the interface is spin active, on the other hand, the conductance spectra depend sensitively on types of the junction and directions of the magnetic moment. In particular, for the current perpendicular to $\boldsymbol{K}_0$, both the normal and the Andreev reflections are suppressed due to the chiral spin structure on the fermi surface. The spin-flip potentials at the interface relax the spin mismatch in the reflection process.

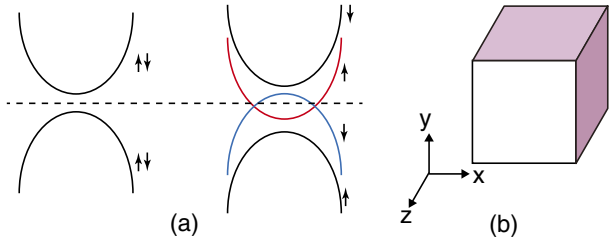

Fig. 1. (Color online) (a) Schematic band structures of theoretical model. The Zeeman effect shifts the bands depending on their spin. We consider two bands on the fermi level indicated by a broken line. (b) We consider two types of junction: current parallel to the z-axis and that parallel to the x. The topological surface states appear on the surfaces perpendicular to the x-axis and those to the y-axis.

2. Weyl Semimetal

To describe the electronic states in Weyl semimetals, we use a simple model given by[10)]

$$H_{\rm W} = \sum_{\alpha,\beta} \int d\boldsymbol{r}\, \psi^\dagger_\alpha(\boldsymbol{r}) \Big[-\frac{\hbar^2}{2m_{\rm W}} (\nabla^2 + k_0^2)\hat{\sigma}_z - i\lambda(\partial_x\hat{\sigma}_x + \partial_y\hat{\sigma}_y) - \mu_{\rm W}\hat{\sigma}_0 \Big]_{\alpha,\beta} \psi_\beta(\boldsymbol{r}), \qquad (1)$$

where $\psi^\dagger_\alpha(\boldsymbol{r})$ ($\psi_\alpha(\boldsymbol{r})$) is the creation (annihilation) operator of an electron with spin α at $\boldsymbol{r}$, ∇ is the three-dimensional Laplacian, $m_{\rm W}$ is the effective mass of an electron, λ denotes the coupling constant of the spin–orbit interaction, and $\mu_{\rm W}$ is the chemical potential measured from the Weyl point. We originally begin with the spin-degenerate two-band model as shown in Fig. 1(a). The Zeeman field decreases (increases) the energy of the spin-up (spin-down) band. Large enough Zeeman fields result in the inverted band structure. The effects of the Zeeman field is taken into account through k_0 in Eq. (1). The Pauli's matrices $\hat{\sigma}_j$ for $j = x$, y, and z represent the real spins of an electron. The unit matrix in spin space is $\hat{\sigma}_0$. By neglecting the two bands away from the fermi level, the electric structure are described by Eq. (1). In the Fourier representation, Eq. (1) becomes

$$H_{\rm W}(\boldsymbol{k}) = \begin{bmatrix} \epsilon_{\boldsymbol{k}} - \mu_{\rm W} & \lambda(k_x - ik_y) \\ \lambda(k_x + ik_y) & -\epsilon_{\boldsymbol{k}} - \mu_{\rm W} \end{bmatrix}, \tag{2}$$

with $\epsilon_{\boldsymbol{k}} = (\hbar^2/2m_{\rm W})(\boldsymbol{k}^2 - k_0^2)$. The energy dispersion and the wave functions are obtained as

$$\begin{pmatrix} \alpha_{\boldsymbol{k}} \\ \beta_{\boldsymbol{k}}(k_x + ik_y)/p \end{pmatrix}, \quad \begin{pmatrix} -\beta_{\boldsymbol{k}}(k_x - ik_y)/p \\ \alpha_{\boldsymbol{k}} \end{pmatrix}, \tag{3}$$

for $E^{\rm W}_{\boldsymbol{k}} - \mu_{\rm W}$ and $-E^{\rm W}_{\boldsymbol{k}} - \mu_{\rm W}$, respectively. Here we define following quantities,

$$E^{\rm W}_{\boldsymbol{k}} = \sqrt{\epsilon^2_{\boldsymbol{k}} + (\lambda p)^2}, \quad \boldsymbol{p} = (k_x, k_y, 0), \tag{4}$$

$$\alpha_{\boldsymbol{k}} = \sqrt{\frac{1}{2}\left(1 + \frac{\epsilon_{\boldsymbol{k}}}{E^{\rm W}_{\boldsymbol{k}}}\right)}, \quad \beta_{\boldsymbol{k}} = \sqrt{\frac{1}{2}\left(1 - \frac{\epsilon_{\boldsymbol{k}}}{E^{\rm W}_{\boldsymbol{k}}}\right)}. \tag{5}$$

The two Weyl points appear at $\pm\boldsymbol{K}_0$. When we consider low energy transport around the chemical potential, the energy band with $E^{\rm W}_{\boldsymbol{k}} - \mu_{\rm W}$ carries the electric current. The group velocity of Weyl semimetal is anisotropic. The velocities are represented by

$$v_{x(y)} = \frac{\hbar k_{x(y)}}{m_{\rm W}} \frac{\epsilon_{\boldsymbol{k}}}{E^{\rm W}_{\boldsymbol{k}}} + \frac{\lambda^2 k_{x(y)}}{\hbar E^{\rm W}_{\boldsymbol{k}}}, \quad v_z = \frac{\hbar k_z}{m_{\rm W}} \frac{\epsilon_{\boldsymbol{k}}}{E^{\rm W}_{\boldsymbol{k}}}, \tag{6}$$

in the $x(y)$ and the z-direction, respectively. In addition, the expectation value of spin $\boldsymbol{S} = (\hbar/2)\hat{\boldsymbol{\sigma}}$ are calculated to be

$$\langle S_{x(y)} \rangle = \frac{\lambda k_{x(y)}}{E^{\rm W}_{\boldsymbol{k}}}, \quad \langle S_z \rangle = \frac{\epsilon_{\boldsymbol{k}}}{E^{\rm W}_{\boldsymbol{k}}}, \tag{7}$$

in units of $\hbar/2$.

The Hamiltonian in the hole space is represented by $-H^*_{\rm W}(-\boldsymbol{k})$. The wave function at $E = -E_{\boldsymbol{k}} + \mu_{\rm W}$ is given by

$$\begin{pmatrix} \alpha_{\boldsymbol{k}} \\ -\beta_{\boldsymbol{k}}(k_x - ik_y)/p \end{pmatrix}. \tag{8}$$

The spin expectation values are calculated to be

$$\langle S_{x(y)} \rangle = \frac{-\lambda k_{x(y)}}{E^{\rm W}_{\boldsymbol{k}}}, \quad \langle S_z \rangle = \frac{\epsilon_{\boldsymbol{k}}}{E^{\rm W}_{\boldsymbol{k}}}, \tag{9}$$

in the hole space.

2.1 *Fermi surface*

To study transport properties unique to the Weyl semimetals, we need to set the chemical potential $\mu_{\rm W}$ to be small enough values. We show the shape of the fermi surface at $\lambda = 0.5\epsilon_0$ for several $\mu_{\rm W}$ in Fig. 2, where the line connects the equal energy points in the Brillouin zone. For $\mu_{\rm W}/\epsilon_0 < 0.4$, the two disconnected fermi surfaces enclose the two Weyl points at $(0, 0, \pm k_0)$. We only show the fermi surface around $\boldsymbol{K}_0 = (0, 0, k_0)$ in Fig. 2. At $\mu_{\rm W}/\epsilon_0 = 0.2$, the shape of fermi surface is still distorted. The fermi surface becomes more ellipsoidal for smaller $\mu_{\rm W}$. In this paper, we fix the parameters as $\lambda = 0.5\epsilon_0$ and $\mu_{\rm W} = 0.1\epsilon_0$.

2.2 *Wave function at a fixed energy*

It is possible to consider two types of junction: (i) the current in the z-direction and (ii) the current in the x-direction. We first discuss the wave function for the current in the z-direction. At an energy $E > 0$, such wave function in the z-direction proportional to $e^{i(k_x x + k_y y)}$ is described by

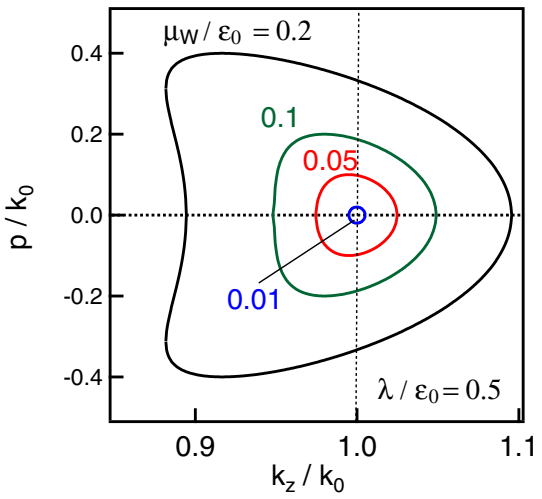

Fig. 2. (Color online) The fermi surface around $\boldsymbol{K}_0$ are plotted at $\lambda/\epsilon_0 = 0.5$ for several $\mu_{\rm W}$. The shape of the fermi surface is independent of the direction of momenta $\boldsymbol{p} = (k_x, k_y, 0)$ in the xy plane.

$$\begin{aligned} \Psi_{\rm W}(z \le 0) = {} & \frac{1}{z^{\rm e}_+} \begin{bmatrix} f^z_{\rm e} \\ \gamma_+ \\ 0 \\ 0 \end{bmatrix} (e^{ik^+_{\rm e} z} a^+ + e^{-ik^+_{\rm e} z} A^+) \\ & + \frac{1}{z^{\rm e}_-} \begin{bmatrix} \gamma_- \\ f^z_{\rm e} \\ 0 \\ 0 \end{bmatrix} (e^{-ik^-_{\rm e} z} a^- + e^{ik^-_{\rm e} z} A^-) \\ & + \frac{1}{z^{\rm h}_+} \begin{bmatrix} 0 \\ 0 \\ f^z_{\rm h} \\ -\gamma_- \end{bmatrix} (e^{-ik^+_{\rm h} z} b^+ + e^{ik^+_{\rm h} z} B^+) \\ & + \frac{1}{z^{\rm h}_-} \begin{bmatrix} 0 \\ 0 \\ -\gamma_+ \\ f^z_{\rm h} \end{bmatrix} (e^{ik^-_{\rm h} z} b^- + e^{-ik^-_{\rm h} z} B^-), \end{aligned} \tag{10}$$

$$f^z_{\rm e(h)} = \mu_{\rm W} + (-)E + \sqrt{D^z_{\rm e(h)}}, \quad \gamma_\pm = \lambda(k_x \pm ik_y), \tag{11}$$

$$k^\pm_{\rm e(h)} = \sqrt{k_0^2 - p^2 \pm (2m_{\rm W}/\hbar^2)\sqrt{D^z_{\rm e(h)}}}, \tag{12}$$

$$D^z_{\rm e(h)} = \{\mu_{\rm W} + (-)E\}^2 - (\lambda p)^2, \tag{13}$$

where $z^{\rm e}_\pm$ and $z^{\rm h}_\pm$ are factors which normalize the wave functions. The coefficients $a^\pm$ ($b^\pm$) are the amplitudes of wave function incoming into the junction interface as an electron (hole). While $A^\pm$ ($B^\pm$) are the amplitudes of wave function outgoing from the junction interface as an electron (hole). We note that $E^{\rm W}_{\boldsymbol{k}}$ was replaced by $\mu_{\rm W} + E$ in the electron space. At the same time, $\epsilon_{\boldsymbol{k}}$ was replaced by $\pm D^z_{\rm e}$ for $k^\pm_{\rm e}$ channel. In the hole space, we have applied relations $E^{\rm W}_{\boldsymbol{k}} \to \mu_{\rm W} - E$ and $\epsilon_{\boldsymbol{k}} \to \pm D^z_{\rm h}$ for $k^\pm_{\rm h}$ channel. In this way, we obtain Eq. (10).

When the current flows in the x-direction, on the other hand, the wave function in the x-direction proportional to $e^{i(k_y y + k_z z)}$ becomes

$$\Psi_{\rm W}(x\le 0)=\frac{1}{z_{k_{\rm e}^+}}\begin{bmatrix} f^x_{{\rm e},+}\\ \gamma_{k_{\rm e}^+,+}\\ 0\\ 0\end{bmatrix}e^{ik_{\rm e}^+x}a^+ +\frac{1}{z_{-k_{\rm e}^-}}\begin{bmatrix}\gamma_{-k_{\rm e}^-,-}\\ f^x_{{\rm e},-}\\ 0\\ 0\end{bmatrix}e^{-ik_{\rm e}^-x}a^-$$
$$+\frac{1}{z_{-k_{\rm e}^+}}\begin{bmatrix} f^x_{{\rm e},+}\\ \gamma_{-k_{\rm e}^+,+}\\ 0\\ 0\end{bmatrix}e^{-ik_{\rm e}^+x}A^+ +\frac{1}{z_{k_{\rm e}^-}}\begin{bmatrix}\gamma_{k_{\rm e}^-,-}\\ f^x_{{\rm e},-}\\ 0\\ 0\end{bmatrix}e^{ik_{\rm e}^-x}A^-$$
$$+\frac{1}{z_{-k_{\rm h}^+}}\begin{bmatrix} 0\\ 0\\ f_{{\rm h},+}\\ -\gamma_{-k_{\rm h}^+,-}\end{bmatrix}e^{-ik_{\rm h}^+x}b^+ +\frac{1}{z_{k_{\rm h}^-}}\begin{bmatrix}0\\ 0\\ -\gamma_{k_{\rm h}^-,+}\\ f_{{\rm h},-}\end{bmatrix}e^{ik_{\rm h}^-x}b^-$$
$$+\frac{1}{z_{k_{\rm h}^+}}\begin{bmatrix} 0\\ 0\\ f_{{\rm h},+}\\ -\gamma_{k_{\rm h}^+,-}\end{bmatrix}e^{ik_{\rm h}^+x}B^+ +\frac{1}{z_{-k_{\rm h}^-}}\begin{bmatrix}0\\ 0\\ -\gamma_{-k_{\rm h}^-,+}\\ f_{{\rm h},-}\end{bmatrix}e^{-ik_{\rm h}^-x}B^-, \tag{14}$$

$$f^x_{{\rm e(h)},\pm}=\mu_{\rm W}+(-)E+\sqrt{D^x_{\rm e(h)}}\mp\lambda k_0\tilde{\lambda}^2/2, \tag{15}$$

$$k^\pm_{\rm e(h)}=\sqrt{A_0\pm(2m_{\rm W}/\hbar^2)\sqrt{D^x_{\rm e(h)}}}, \tag{16}$$

$$\gamma_{k,\pm}=\lambda(k\pm ik_y),\quad \tilde{\lambda}=\lambda k_0/\epsilon_0,\quad \epsilon_0=\hbar^2k_0^2/(2m_{\rm W}), \tag{17}$$

$$A_0=k_0^2-k_y^2-k_z^2-k_0^2\tilde{\lambda}^2/2, \tag{18}$$

$$D^x_{\rm e(h)}=\lambda^2(k_z^2-k_0^2)+(\lambda k_0)^2\tilde{\lambda}^2/4+\{\mu_{\rm W}+(-)E\}^2. \tag{19}$$

On the way to Eq. (14), we have used relations $E_{\boldsymbol{k}}\to\mu_{\rm W}+E$ and $\epsilon_{\boldsymbol{k}}\to-\tilde{\lambda}\lambda k_0/2\pm\sqrt{D^x_{\rm e}}$ for $k^\pm_{\rm e}$ channel in the electron space. In the hole space, we have applied $E_{\boldsymbol{k}}\to\mu_{\rm W}-E$ and $\epsilon_{\boldsymbol{k}}\to-\tilde{\lambda}\lambda k_0/2\pm\sqrt{D^x_{\rm h}}$ for $k^\pm_{\rm h}$ channel.

2.3 Surface bound states

The topologically protected surface bound states appear at the surfaces perpendicular to the x-axis and those perpendicular to the y-axis. However it is absent on the surface perpendicular to the z-axis. It is possible to study the spectra of such topological surface states by using the wave function in Eq. (14). In the electron space, the wave function of the bound states neat the surface (i.e., $x=0$) can be described by

$$\Psi^{\rm e}_{\rm W}(x)=\begin{bmatrix} f^x_{{\rm e},+}\\ \gamma_{-k_{\rm e}^+,+}\end{bmatrix}e^{-ik_{\rm e}^+x}A^+ +\begin{bmatrix}\gamma_{k_{\rm e}^-,-}\\ f^x_{{\rm e},-}\end{bmatrix}e^{ik_{\rm e}^-x}A^-. \tag{20}$$

These two wave functions represent the wave decaying into the Weyl semimetal ($x<0$) for $D^x_{\rm e}<0$. The condition $D^x_{\rm e}<0$ results in the complex wave number in the x-direction. By imposing the boundary condition $\Psi^{\rm e}_{\rm W}(0)=0$, we obtain the dispersion of the surface bound states as $E_{\rm BS}=\lambda k_y-\mu_{\rm W}$ for $k_y^2<k_0^2(1-\tilde{\lambda}^2/4)-k_z^2$. Thus chiral electric current flows in the y-direction. The wave function of the bound states are obtained as

$$\Psi_{\rm BS}(x)=C_0e^{\tilde{\lambda}k_0x/2}\sin(\sqrt{k_0^2-k_z^2-k_y^2}x)\begin{pmatrix}\delta_0\\ \delta_0^*\end{pmatrix}, \tag{21}$$

for $x<0$, where $\delta_0=e^{i\pi/4}$ and C_0 is a constant. We have used a relation $\tilde{\lambda}\ll 1$. The bound states are the eigen states of $\hat{\sigma}_y$. At $k_y=\mu/\lambda$, a bound state appears on the fermi level. Due to the complex wave number under $D^x_{\rm e}<0$, unfortunately, the surface bound state does not contribute to the electric transport in the x-direction. In the ballistic regime, the wave numbers in the parallel directions to the interface are conserved in the transmission and the reflection processes. An electron incoming into the interface through a propagation channel cannot be reflected or transmitted via the bound state. This is because the bound states is formed by the decaying waves belonging to the evanescent channel.

2.4 Junction with a superconductor

The Hamiltonian in a metallic superconductor is represented in the momentum space,

$$H_{\rm S}(\boldsymbol{k})=\begin{bmatrix}\xi_{\boldsymbol{k}}\hat{\sigma}_0 & \Delta i\hat{\sigma}_y\\ -\Delta i\hat{\sigma}_y & -\xi^*_{-\boldsymbol{k}}\hat{\sigma}_0\end{bmatrix}, \tag{22}$$

$$\xi_{\boldsymbol{k}}=\frac{\hbar^2\boldsymbol{k}^2}{2m_{\rm S}}-\mu_{\rm S}, \tag{23}$$

where Δ is the amplitude of the pair potential, and $m_{\rm S}$ ($\mu_{\rm S}$) is the mass of an electron (the chemical potential) in the superconductor. The wave function in the z-direction, for example, is represented by

$$\Psi_{\rm S}(z)=\begin{bmatrix}u_0\hat{\sigma}_0\\ v_0(-i\hat{\sigma}_y)\end{bmatrix}\begin{pmatrix}C_\uparrow\\ C_\downarrow\end{pmatrix}e^{iq^{\rm e}z} +\begin{bmatrix}v_0(i\hat{\sigma}_y)\\ u_0\hat{\sigma}_0\end{bmatrix}\begin{pmatrix}D_\uparrow\\ D_\downarrow\end{pmatrix}e^{-iq^{\rm h}z}, \tag{24}$$

$$u_0 = \sqrt{\frac{1}{2}\left(1+\frac{\Omega}{E}\right)}, \quad v_0 = \sqrt{\frac{1}{2}\left(1-\frac{\Omega}{E}\right)}, \tag{25}$$

$$\Omega = \sqrt{E^2-\Delta^2}, \quad q^{\mathrm{e(h)}} = \sqrt{k_F^2 - p^2 + (-)2m_{\mathrm{S}}\Omega/\hbar^2}. \tag{26}$$

The wave functions on either sides of the junction are connected by the boundary conditions,

$$\Psi_{\mathrm{W}}(z=0) = \Psi_{\mathrm{S}}(z=0), \tag{27}$$

$$-\frac{\hbar^2}{2m_{\mathrm{W}}}\begin{bmatrix}\hat{\sigma}_z & 0\\ 0 & \hat{\sigma}_z\end{bmatrix}\partial_z\Psi_{\mathrm{W}}(z)\Big|_{z=0} = -\frac{\hbar^2}{2m_{\mathrm{S}}}\partial_z\Psi_{\mathrm{S}}(z)\Big|_{z=0} + [V_0\hat{\sigma}_0 + \boldsymbol{V}\cdot\hat{\boldsymbol{\sigma}}]\Psi_{\mathrm{S}}(z=0), \tag{28}$$

for the current in the z-direction. Here we introduce the barrier potential $V_0\delta(z)$ and the magnetic potential $\boldsymbol{V}\cdot\hat{\boldsymbol{\sigma}}\delta(z)$ at the interface. For the current in the x-direction, we change z to x in the above conditions. In addition to this, we need to add

$$\frac{\lambda}{2i}\begin{bmatrix}\hat{\sigma}_x & 0\\ 0 & -\hat{\sigma}_x\end{bmatrix}\Psi_{\mathrm{W}}(x=0) \tag{29}$$

on the left hand side of Eq. (28) to satisfy the current conservation law. By using the boundary conditions in Eqs. (27) and (28), it is possible to obtain the reflection matrix,

$$\begin{bmatrix}A^+\\ A^-\\ B^+\\ B^-\end{bmatrix} = \begin{bmatrix}\hat{r}_{\mathrm{ee}} & \hat{r}_{\mathrm{eh}}\\ \hat{r}_{\mathrm{he}} & \hat{r}_{\mathrm{hh}}\end{bmatrix}\begin{bmatrix}a^+\\ a^-\\ b^+\\ b^-\end{bmatrix}. \tag{30}$$

The differential conductance of the junction is calculated as[28,29]

$$G_{\mathrm{WS}}(eV) = \frac{e^2}{h}\sum_{\boldsymbol{P}}\mathrm{Tr}[\hat{1}_{\mathrm{ee}} - \hat{R}_{\mathrm{ee}}\hat{R}_{\mathrm{ee}}^\dagger + \hat{R}_{\mathrm{he}}\hat{R}_{\mathrm{he}}^\dagger]\Big|_{E=eV}, \tag{31}$$

$$\hat{R}_{\mathrm{ee}} = \begin{pmatrix}\sqrt{v_{\mathrm{e}}^+} & 0\\ 0 & \sqrt{v_{\mathrm{e}}^-}\end{pmatrix}\hat{r}_{\mathrm{ee}}\begin{pmatrix}1/\sqrt{v_{\mathrm{e}}^+} & 0\\ 0 & 1/\sqrt{v_{\mathrm{e}}^-}\end{pmatrix}, \tag{32}$$

$$\hat{R}_{\mathrm{he}} = \begin{pmatrix}\sqrt{v_{\mathrm{h}}^+} & 0\\ 0 & \sqrt{v_{\mathrm{h}}^-}\end{pmatrix}\hat{r}_{\mathrm{he}}\begin{pmatrix}1/\sqrt{v_{\mathrm{e}}^+} & 0\\ 0 & 1/\sqrt{v_{\mathrm{e}}^-}\end{pmatrix}, \tag{33}$$

$$\hat{1}_{\mathrm{ee}} = \begin{pmatrix}s_{\mathrm{e}}^+ & 0\\ 0 & s_{\mathrm{e}}^-\end{pmatrix}, \tag{34}$$

where $v_{\mathrm{e}}^\pm$ ($v_{\mathrm{h}}^\pm$) is the velocity of $k_{\mathrm{e}}^\pm$ ($k_{\mathrm{h}}^\pm$) channel at the electron (hole) space in the Weyl semimetal and $\boldsymbol{P}$ denotes the momenta parallel to the interface. We define that $s_{\mathrm{e}}^\pm$ is 1 for the propagating $k_{\mathrm{e}}^\pm$ channel and 0 for the evanescent $k_{\mathrm{e}}^\pm$ channel in the electron space.

3. Differential Conductance

Throughout this paper, we fix material parameters in the superconductor as $m_{\mathrm{S}} = m_{\mathrm{W}}$ and $\mu_{\mathrm{S}} = 2\epsilon_0$. These parameters only modify the transmission probability of the junction. The amplitude of the pair potential is fixed at $\Delta = 0.01\epsilon_0$ which gives the smallest energy scale in our model. As we discussed in Sect. 2.1, we choose $\mu_{\mathrm{W}} = 0.1\epsilon_0$ and $\lambda = 0.5\epsilon_0$ in the Weyl semimetal. The barrier potentials are parameterized as $z_0 = (m_{\mathrm{W}}/\hbar^2 k_0)V_0$ and $\boldsymbol{M} = (m_{\mathrm{W}}/\hbar^2 k_0)\boldsymbol{V}$.

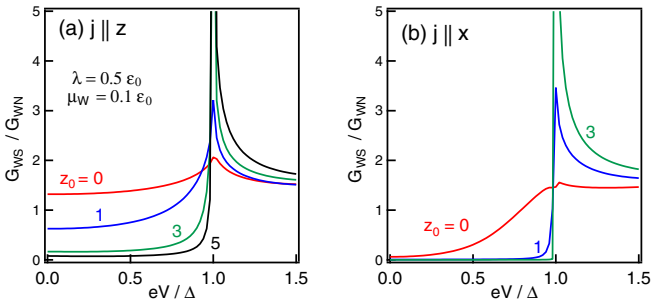

Fig. 3. (Color online) The differential conductance of Weyl-semimetal/superconductor junction is plotted as a function of the bias voltage for the current parallel to the z-axis in (a) and for the current parallel to the x-axis in (b). Here we choose $mu_{\mathrm{W}} = \mu_{\mathrm{S}}$, $\mu_{\mathrm{S}} = 2\epsilon_0$, $\lambda = 0.5\epsilon_0$, and $\mu_{\mathrm{W}} = 0.1\epsilon_0$.

We first discuss the differential conductance without magnetic barrier at the interface (i.e., $\boldsymbol{M} = 0$). Figure 3 shows the differential conductance of Weyl-semimetal/superconductor junction for the current parallel to the z-axis in (a) and that for the current parallel to the x-axis in (b). The results are normalized to the conductance of Weyl-semimetal/normal-metal junction (G_{WN}) at $eV = 0$. The all results in (a) and (b) show the dip structure below the gap because the transmission probability of the junction is less than unity even at $z_0 = 0$ reflecting the difference in the band structure between the Weyl semimetal and the superconductor. The transmission probability T_N in the normal state is 0.76, 0.48, 0.16, and 0.076 for $z_0 = 0$, 1, 3, and 5, respectively in (a). In (b), T_N is 0.71, 0.31, and 0.05 for $z_0 = 0$, 1, and 3, respectively. The gap structure becomes clearer when we decrease T_N by increasing z_0. Such behaviors are well known in the conductance spectra in normal-metal/superconductor junctions. At the first glance, we cannot find any characteristic features of Weyl semimetals in Fig. 3.

The results, however, reflect the characteristic spin configuration of Weyl semimetals. In Fig. 4, we illustrate the spin configuration on the fermi surface for the two types of junction. When the current is parallel to the z-direction as shown in (a), an electron goes into the interface from the two fermi surface near $\pm K_0$. Here we focus on an electron wave incoming from $k_z = k_{\mathrm{e}}^+ > 0$ channel as enclosed by the dotted rectangular. The spin calculated from Eq. (7) are

$$\boldsymbol{S}(k_x, k_y, k_{\mathrm{e}}^+) = \left(\frac{\lambda k_x}{\mu_{\mathrm{W}}+E}, \frac{\lambda k_y}{\mu_{\mathrm{W}}+E}, \frac{\sqrt{D_{\mathrm{e}}^z}}{\mu_{\mathrm{W}}+E}\right), \tag{35}$$

for an incoming electron at $k_z = k_{\mathrm{e}}^+$. The wave numbers in the z-direction for outgoing channel in the electron space are k_{e}^- and $-k_{\mathrm{e}}^+$. The former is in the same fermi surface as that in the incident wave, whereas the latter belongs to the opposite fermi surface. In such outgoing channels, S_x and S_y remain unchanged from those in the incoming one. However, $S_z = \sqrt{D_{\mathrm{e}}^z}/(\mu_{\mathrm{W}}+E)$ and $-\sqrt{D_{\mathrm{e}}^z}/(\mu_{\mathrm{W}}+E)$ for $-k_{\mathrm{e}}^+$ and k_{e}^-, respectively. In Fig. 4(a), the direction of spin within xz spin plane is illustrated by arrows on the fermi surface at $k_y = 0$. It is possible to obtain the same spin configuration within yz plane at $k_x = 0$. Due to the spin mismatch in S_z, the normal reflection to k_{e}^- is basically suppressed. To conserve the spin direction, therefore, an electron incoming at k_{e}^+ is reflected into $-k_{\mathrm{e}}^+$ in the normal reflection. In the outgoing channels in the hole space, the spin becomes

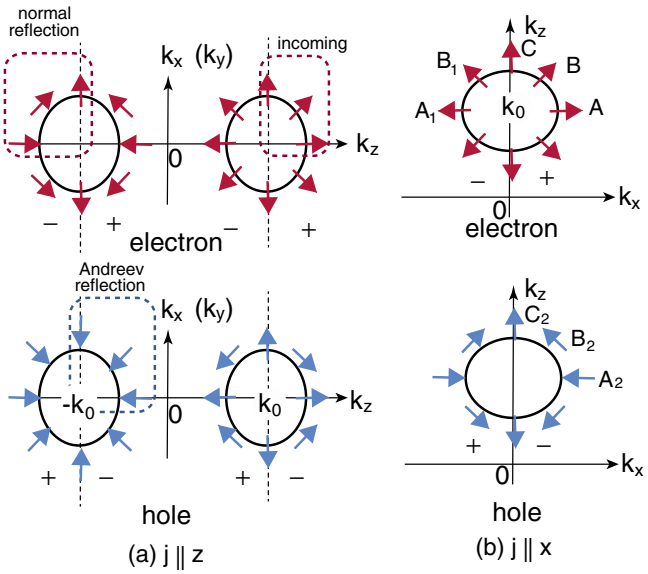

Fig. 4. (Color online) Spin configuration on the fermi surface within xz plane in spin space. In the junction for the current parallel to z, an electron is incident from the two fermi surfaces near $(0, 0, \pm k_0)$ having the opposite spin chiral texture to each other as shown in (a). For the current parallel to x in (b), an electron is reflected into the same fermi surface because k_y and k_z are conserved due to the translational symmetry in yz plane. We only show the spin configuration on the fermi surface around $(0, 0, k_0)$ in (b). The spin is conserved in the normal reflection and it becomes opposite direction in the Andreev reflection. The $+(-)$ in the bottom of figures indicates the sign of the velocity in the current direction.

$$\boldsymbol{S}(k_x, k_y, k_{\rm h}^+) = \left(\frac{-\lambda k_x}{\mu_{\rm W} - E}, \frac{-\lambda k_y}{\mu_{\rm W} - E}, \frac{\sqrt{D_{\rm h}^z}}{\mu_{\rm W} - E}\right) \tag{36}$$

at $k_z = k_{\rm h}^+$, and

$$\boldsymbol{S}(k_x, k_y, -k_{\rm h}^-) = \left(\frac{-\lambda k_x}{\mu_{\rm W} - E}, \frac{-\lambda k_y}{\mu_{\rm W} - E}, \frac{-\sqrt{D_{\rm h}^z}}{\mu_{\rm W} - E}\right) \tag{37}$$

at $k_z = -k_{\rm h}^-$. For $E \sim \Delta \ll \mu_{\rm W}$, S_x and S_y components in the hole space are almost opposite to those in the incoming electron. However, S_z component depends on the outgoing channels. The Andreev reflection flips the spin of an incoming electron because we assume the spin-singlet superconductor. Thus the Andreev reflection is possible at $-k_{\rm h}^-$ belonging to the opposite fermi surface. An incident electron from one fermi surface is reflected in to the opposite fermi surface without suffering the spin mismatch. In the junction for the current parallel to z-direction, therefore, the reflection processes are as usual as those in the normal metal. We note that there is no spin mismatch in the S_y component.

The situation in the junction for the current parallel to the x is more complicated. The spin of an incoming electron at $k_x = k_{\rm e}^+ > 0$ channel is

$$\boldsymbol{S}(k_{\rm e}^+, k_y, k_z) = \frac{1}{\mu_{\rm W} + E}\left(\lambda k_{\rm e}^+, \lambda k_y, -\frac{\tilde{\lambda}\lambda k_0}{2} + \sqrt{D_{\rm e}^x}\right). \tag{38}$$

On the other hand, they are

$$\boldsymbol{S}(-k_{\rm e}^+, k_y, k_z) = \frac{1}{\mu_{\rm W} + E}\left(-\lambda k_{\rm e}^+, \lambda k_y, -\frac{\tilde{\lambda}\lambda k_0}{2} + \sqrt{D_{\rm e}^x}\right), \tag{39}$$

in the normal reflection at $k_x = -k_{\rm e}^+$ in the electron space, and

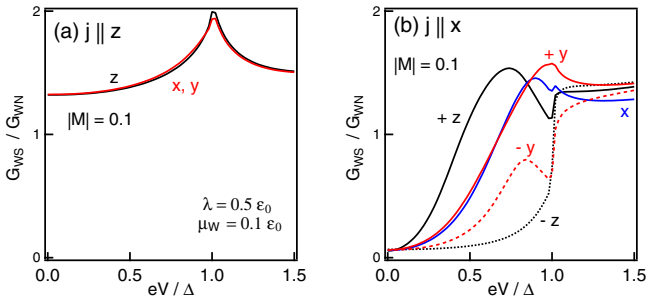

Fig. 5. (Color online) The differential conductance is plotted as a function of the bias voltage for the current parallel to the z-axis in (a) and for the current parallel to the x-axis in (b). We introduce the magnetic barrier at $|\boldsymbol{M}| = 0.1$. Here we choose $z_0 = 0$, $\mu_{\rm W} = 0.1\epsilon_0$ and $\lambda = 0.5\epsilon_0$.

$$\boldsymbol{S}(k_{\rm h}^+, k_y, k_z) = \frac{1}{\mu_{\rm W} - E}\left(-\lambda k_{\rm h}^+, -\lambda k_y, -\frac{\tilde{\lambda}\lambda k_0}{2} + \sqrt{D_{\rm h}^x}\right), \tag{40}$$

in the Andreev reflection at $k_x = k_{\rm h}^+ > 0$ in the hole space. Although the S_y component always satisfies the spin selection rule, S_x and S_z components violate the selection rule depending on the incident angle. In Fig. 4(b), the spin configuration within xz spin plane is illustrated by arrows on the fermi surface. We only show the spin structure on the fermi surface around $k_z = k_0$ because the wave number in the yz plane is conserved in the reflection process. When the incident electron has a wave number as indicated by A in Fig. 4(b), the normal reflection to A_1 is suppressed due to the spin mismatch in S_x component but the Andreev reflection to A_2 is possible. On the other hand, when the incident electron has a wave number as indicated by C, the normal reflection to C itself is possible but the Andreev reflection to C_2 is suppressed because of the spin mismatch in S_z component. At the intermediate incident wave number as indicated by B, both the normal and the Andreev reflections are allowed. Therefore the reflection property depends strongly on the incoming wave number. The results in Fig. 3(b) indicate that the Andreev reflection probability is small near the zero-bias because of the spin mismatch in the reflection process. The conductance spectra, however, are expected be sensitive to spin active potential at the interface.

In Fig. 5, we show the conductance spectra in the presence of the spin dependent potential at the interface, where $z_0 = 0$ and $|\boldsymbol{M}| = 0.1$. In (a), results for the current in the z-direction is plotted for three directions of $\boldsymbol{M}$. The conductance spectra are almost unchanged from the results in Fig. 3(a) with $z_0 = 0$ because there is no spin mismatch in the reflection processes. However, the conductance spectra for the current parallel to x depends sensitively on the direction of the magnetic moment $\boldsymbol{M}$. For example, $+z$ and $-z$ mean the magnetic moment points $+z$ and $-z$-direction in spin space, respectively. The conductance for $+x$ and that for $-x$ are identical to each other. The magnetic moment at the interface drastically modifies subgap spectra for the current parallel to x-direction because it relaxes the spin mismatch in both the normal and the Andreev reflection processes.

The conductance spectra also depends on the amplitude of the magnetic moment. In Fig. 6, we show the conductance spectra for $|\boldsymbol{M}| = 0.5$. The peak at $eV = \Delta$ is suppressed by the magnetic moment for the current parallel to z-direction as

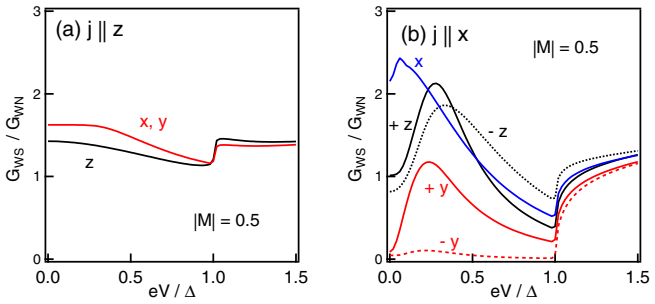

Fig. 6. (Color online) The differential conductance at $|z| = 0.5$. (a): the current parallel to the z-axis. (b): the current parallel to the x-axis.

shown in (a). The subgap spectra are totally smooth function of eV. In (b), on the other hand, the results show a rich variety of the subgap spectra depending on the directions of magnetic moment. In particular, the amplitudes of the conductance around the zero-bias for for $\pm z$ and x are larger than those at $\boldsymbol{M} = 0$ in Fig. 3(b). This means the large amplitude of the Andreev reflection probability.

4. Discussion

The Andreev reflection means the penetration of a Cooper pair into the Weyl semimetal. When the current is parallel to z-direction, the results in Fig. 3(a) are qualitatively the same as those in normal-metal/superconductor junction as we discussed in Sect. 3. Thus a spin-singlet s-wave Cooper pair would be dominant in the semimetal. When the current is parallel to x, on the other hand, the spin-flip scattering assists the Andreev reflection as shown in Figs. 5(b) and 6(b). Thus the spin-triplet Cooper pairs are expected in the Weyl semimetal. In addition to this, the orbital part of a Cooper pair is also modified by the reflection. The junction interface can mix the even-parity and odd-parity components because it breaks the translational invariance. Thus the odd-parity spin-triplet component is expected as well as the even-parity spin-singlet one. Moreover a Cooper pair with odd-frequency symmetry might stay in the Weyl semimetal in the dirty limit.[30,31] To resolve the pairing symmetry, we need calculate the anomalous Green function and analyze it. This would be an interesting issue in the future.

5. Conclusion

We have theoretically studied the differential conductance in the junction of Weyl-semimetal and metallic superconductor. The Weyl semimetals have the two Weyl points in the Brillouin zone at $\pm\boldsymbol{K}_0$ with $\boldsymbol{K}_0 = (0, 0, k_0)$. Therefore, it is possible to consider two different configurations of the junction: the current parallel to z-axis and the current parallel to x one. The characteristic features of the conductance spectra for the current parallel to z are essentially the same as those in the usual normal-metal/superconductor junctions. Namely, the conductance spectra becomes the bulk density of states in the superconductor when the normal transmission probability of the junction is low. In addition, the conductance spectra are insensitive to the weak magnetic moment at the junction interface. In this case, the chiral spin structure on the fermi surface does not affect the reflection process at the interface. In the case of the junction for the current parallel to the x-axis, on the other hand, the chiral spin structure on the fermi surface suppress the Andreev reflection depending on the incident angles of a quasiparticle. This feature is explained by the spin mismatch between the incoming wave and the outgoing ones. The conductance spectra depends sensitively on the direction and the amplitudes of the magnetic moment at the interface because the spin flip scatterings relax the spin mismatch. The topological bound states appear on the xy surface of the Weyl semimetal. They, however, do not affect the low energy transport in the junctions.

Acknowledgment

The authors are grateful to Y. Tanaka for useful discussion. This work was supported by the "Topological Quantum Phenomena" (No. 22103002) Grant-in Aid for Scientific Research on Innovative Areas from the Ministry of Education, Culture, Sports, Science and Technology of Japan (MEXT).

1) S. Murakami, New J. Phys. **9**, 356 (2007).
2) X. Wan, A. M. Turner, A. Vishwanath, and S. Y. Savrasov, Phys. Rev. B **83**, 205101 (2011).
3) A. A. Burkov, M. D. Hook, and L. Balents, Phys. Rev. B **84**, 235126 (2011).
4) A. A. Burkov and L. Balents, Phys. Rev. Lett. **107**, 127205 (2011).
5) G. B. Halász and L. Balents, Phys. Rev. B **85**, 035103 (2012).
6) T. Ojanen, Phys. Rev. B **87**, 245112 (2013).
7) A. A. Zyuzin, S. Wu, and A. A. Burkov, Phys. Rev. B **85**, 165110 (2012).
8) Y. Chen, S. Wu, and A. A. Burkov, Phys. Rev. B **88**, 125105 (2013).
9) H. Wei, S. P. Chao, and V. Aji, Phys. Rev. Lett. **109**, 196403 (2012).
10) K.-Y. Yang, Y.-M. Lu, and Y. Ran, Phys. Rev. B **84**, 075129 (2011).
11) A. A. Zyuzin and A. A. Burkov, Phys. Rev. B **86**, 115133 (2012).
12) P. Hosur, S. A. Parameswaran, and A. Vishwanath, Phys. Rev. Lett. **108**, 046602 (2012).
13) P. E. C. Ashby and J. P. Carbotte, Phys. Rev. B **87**, 245131 (2013).
14) B. Rosenstein and M. Lewkowicz, Phys. Rev. B **88**, 045108 (2013).
15) Y. Ominato and M. Koshino, Phys. Rev. B **89**, 054202 (2014).
16) J. H. Jiang, Phys. Rev. A **85**, 033640 (2012).
17) G. Y. Cho, arXiv:1110.1939.
18) P. Delplace, J. Li, and D. Carpentier, Europhys. Lett. **97**, 67004 (2012).
19) R. E. Simpson, P. Fons, A. V. Kolobov, T. Fukaya, M. Krbal, T. Yagi, and J. Tominaga, Nat. Nanotechnol. **6**, 501 (2011).
20) B. Sa, J. Zhou, Z. Sun, J. Tominaga, and R. Ahuja, Phys. Rev. Lett. **109**, 096802 (2012).
21) M. Neupane, S. Xu, R. Sankar, N. Alidoust, G. Bian, C. Liu, I. Belopolski, T.-R. Chang, H.-T. Jeng, H. Lin, A. Bansil, F. Chou, and M. Z. Hasan, arXiv:1309.7892.
22) S. Borisenko, Q. Gibson, D. Evtushinsky, V. Zabolotnyy, B. Buechner, and R. J. Cava, arXiv:1309.7978.
23) Z. Wang, H. Weng, Q. Wu, X. Dai, and Z. Fang, Phys. Rev. B **88**, 125427 (2013).
24) T. Meng and L. Balents, Phys. Rev. B **86**, 054504 (2012).
25) H. Wei, S. P. Chao, and V. Aji, Phys. Rev. B **89**, 014506 (2014).
26) G. Y. Cho, J. H. Bardarson, Y.-M. Lu, and J. E. Moore, Phys. Rev. B **86**, 214514 (2012).
27) W. Chen, L. Jiang, R. Shen, L. Sheng, B. G. Wang, and D. Y. Xing, Europhys. Lett. **103**, 27006 (2013).
28) G. E. Blonder, M. Tinkham, and T. M. Klapwijk, Phys. Rev. B **25**, 4515 (1982).
29) Y. Takane and H. Ebisawa, J. Phys. Soc. Jpn. **61**, 1685 (1992).
30) F. S. Bergeret, A. F. Volkov, and K. B. Efetov, Phys. Rev. Lett. **86**, 4096 (2001).
31) Y. Asano, Y. Tanaka, and A. A. Golubov, Phys. Rev. Lett. **98**, 107002 (2007).